

Quantum emitters coupled to circular nanoantennas for high brightness quantum light sources

Hamza A. Abudayyeh¹ and Ronen Rapaport^{1,2}

¹ Racah Institute for Physics, and

² Applied Physics Department, The Hebrew University of Jerusalem, Jerusalem 9190401, Israel

Abstract

Engineering the directionality and emission rate of quantum light sources is essential in the development of modern quantum applications. In this work we use numerical calculations to optimize the brightness of a broadband quantum emitter positioned in a hybrid metal-dielectric circular periodic nanoantenna. The optimized structure features a photon collection efficiency of 74% (82%) and a photon flux enhancement of over 10 (6) into a numerical aperture of 0.22 (0.50) respectively, corresponding to a direct coupling into two types of multimode fibers. In order to enhance the emission rate, we present a new circular nanoantenna design where a quantum emitter is attached to a silver nanocone at the center of the antenna. After optimization, we find a collection efficiency of 61% (78%) into a numerical aperture of 0.22 (0.50), giving a brightness enhancement of 1000 (600) for an unpolarized emitter. The enhancements in both structures are broadband due to the low quality factor of the device and are therefore ideal for room-temperature sources. This type of a scalable design can be utilized towards on-chip, high brightness quantum light sources operating at room temperature.

1 Introduction

Single quantum emitters are at the heart of various quantum applications such as quantum computation, encryption, simulations, communications, metrology among many others.[1, 2] As candidates for such applications, many quantum emitters have been studied [3] including trapped atoms [4], single molecules [5], impurity centers (e.g silicon vacancies (SiV) in diamond [6]), nanocrystal colloidal quantum dots (NQDs) [7], and self assembled quantum dots [8].

Two limitations face free-standing quantum emitters however. The first lies in their isotropic angular emission pattern which limits the ability to efficiently

collect their emitted photons. The second is that typical solid state quantum emitters can have low emission rates which will limit the speed of future technologies. In the past decade there have been considerable efforts to solve these deficiencies by modifying the photonic environment near the quantum emitter. [9, 10] To achieve this, emitters were embedded in, or near to various nanostructures. For simplicity, in this work we will refer to any nanostructure that modifies the emission rate or directionality of a quantum emitter as an antenna.

One approach for improving the directionality and emission rate of quantum emitters is the use of metallic antennas. These include metal nanoparticles (MNPs) [9], plasmonic patch antennas [11, 12, 13], metallic nanoslit arrays [14], Yagi-Uda nanoantennas [15, 16] and circular bullseye plasmonic nanoantennas [17, 18]. The advantage of using such structures is that plasmonic modes have low mode volumes accompanied with low quality factors enabling spontaneous emission lifetime shortening and emission redirection over broad spectral ranges which is beneficial for room-temperature broadband sources such as colloidal quantum dots and color centers in diamond [19]. On the other hand, for efficient coupling the emitter has to be placed in the vicinity of the plasmonic structure which will increase nonradiative recombination rates and if placed too close will cause quenching of the emission all together [9].

Another approach is to use pure dielectric antennas such as microcavities [8] and photonic crystals [20, 21, 22] that feature high directionality, high radiative enhancement factors, and low-loss [23, 24]. Despite these advantages however, dielectric antennas usually come with a limiting narrow frequency bandwidth that is usually unsuitable for room temperature quantum emitters [25], and are much more complex to fabricate.

Therefore a hybrid metal-dielectric nanoantenna that combines the advantages of metallic and dielectric antennas but with much less of their drawbacks was developed. In such a design, the emitter can be placed at a large distance from the metal and still produce high directionality in a broad spectral range [26, 27]. Our recent experiments demonstrated that the single photons emitted from a single nanocrystal quantum dot (NQD) positioned in such a hybrid circular ('bullseye') antenna can be collected with an efficiency of around 37% into a moderate numerical aperture (NA) of 0.65. Furthermore, the ability of positioning a single NQD at the hotspot of the antenna was developed which enables fabrication of highly directional room-temperature single photon sources [27, 28].

While this points into a promising direction the system should be further optimized to enhance both the collection efficiency and decay rate of a quantum emitter. This optimization is crucial for applications such as quantum key distribution, single shot readouts of nitrogen vacancy (NV) centers, sensing applications, and random number generation [29, 3, 30, 31] some of which will be discussed further below. It is therefore pivotal to develop an antenna that combines both high collection efficiencies and high decay rate enhancement. Another drawback of the previous design was the plasmonic emission due to the metal corrugation near the quantum emitter which reduced the single photon purity of the source. [27] Consequently it would be desirable, for single photon

sources at least, that the central area lying within the focus of the exciting laser be flat.

In this work we introduce a new hybrid circular antenna where the emitter is positioned in proximity to a central metal cone at the center of the bullseye antenna, and use a finite-difference time-domain (FDTD) method [32, 33] to optimize the brightness of the emitter into low NA's, with the goal to have a high brightness broadband source of single photons directly coupled to a fiber, without the need of any additional collimating optics. This is achieved by simultaneously optimizing the emission directionality and the enhancement of the emission rate of a dipole emitter. The particle swarm algorithm [34] was used for the optimization process.

In section 2 we define relevant quantities to be optimized, such as the collection efficiency and the enhancement factors of the emitters brightness. In section 3 and 4 we will introduce two optimized designs for a bullseye antenna without and with a central enhancing element respectively.

2 General definitions: coupling between a dipole emitter and an antenna

The decay rate of a dipole emitter Γ in an inhomogeneous environment will depend on the orientation of the dipole moment with respect to the polarization of the electromagnetic modes. Thus in general the response of an antenna will vary for different dipole orientations and therefore we will label all subsequent quantities with an index $i = x, y, z$ that represents the dependence on the dipole orientation with respect to some coordinate system. For an emitter in free space the local density of states is isotropic and the decay rate reduces to Γ_{0i} . This intrinsic decay rate in general includes both radiative (Γ_{0i}^r) and non-radiative (Γ_{0i}^{nr}) decay rates. Intrinsic non-radiative loss mechanisms vary for different emitters and include for example phonon-scattering [35], Auger recombination of multiexcitons in colloidal quantum dots, [36], and losses to lattice defects in color centers [6].

In a modified environment the decay rate (Γ_i) changes and the Purcell factor is defined as [37]:

$$F_i = \frac{\Gamma_i}{\Gamma_{0i}}. \quad (1)$$

where $F_i = F(\mu_i)$ and $\Gamma_i = \Gamma(\mu_i)$ and so on represents the dependence of these quantities on the dipole orientation as discussed above. This factor determines the reduction ($F_i > 1$) or increase ($F_i < 1$) of the intrinsic lifetime of the emitter due to the modified electromagnetic environment and in general does not equal the enhancement of the emitter's emission into the far-field since part of the emission can be channeled into non-radiative losses in the antenna (such as Joule losses in metals). Thus we define a radiative enhancement factor F_i^r as the net increase of total photon flux while the non-radiative enhancement factor F_i^{nr} depicts the leakage of emission into lossy modes of the antenna (therefore

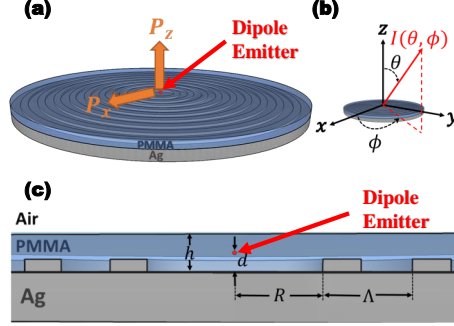


Figure 1: (a) Schematic representation of the hybrid metallic dielectric bullseye nanoantenna with empty central area displaying the two independent dipole orientations. (b) The azimuthal (ϕ) and polar (θ) angles of the far field intensity distribution. (c) Cross section of the nanoantenna defining the key geometric parameters: the central cavity radius (R), groove period (Λ), emitter height (d), and polymer thickness (h)

modifying the non-radiative decay rate). Note that the antenna in most cases doesn't affect the intrinsic non-radiative decay rate and thus we can write the total decay rate as:

$$\Gamma_i = F_i \Gamma_{0i} = \underbrace{F_i^r \Gamma_{0i}^r}_{\Gamma_i^r} + \underbrace{F_i^{nr} \Gamma_{0i}^r + \Gamma_{0i}^{nr}}_{\Gamma_i^{nr}} \quad (2)$$

In free space the intrinsic quantum yield $QY_{0i} = \Gamma_{0i}^r / \Gamma_{0i}$ defines the probability that the photon is emitted into the far-field. The presence of an antenna in general will modify the radiative and non-radiative decay rates and therefore the overall quantum yield of an antenna-emitter system $QY_i = \Gamma_i^r / \Gamma_i$ is altered and can be written as:

$$QY_i = \frac{F_i^r}{F_i} QY_{0i} \quad (3)$$

The effect of the antenna on the quantum yield depends on the intrinsic features of the dipole ($\Gamma_{0i}^r, \Gamma_{0i}^{nr}$) and antenna (F_i^r, F_i^{nr}) in a coupled fashion since F_i is defined as in equation 2. In this work we will be considering a dipole emitter with unity intrinsic quantum yield and therefore F_i reduces to $F_i^r + F_i^{nr}$ and we can define an antenna quantum efficiency $AE = F_i^r / F_i$ which is independent of the properties of the dipole emitter.

Another interesting property of the emitter-antenna system is the far-field brightness. An emitter with an intrinsic radiative decay rate (Γ_{0i}^r) will have a total far field brightness denoted by Φ_{0i}^{tot} (*tot* refers to integration over all angles), that is dependent on the excitation power. We define the brightness of the emitting system as the flux that is emitted into a certain collection cone of given NA , given by:

$$\Phi_i(\theta_{NA}) = \Phi_{0i}^{tot} F_i^r \eta_i(\theta_{NA}) \quad (4)$$

where $\eta_i(\theta_{NA})$ is the collection efficiency which quantifies the directionality of the emitting system and can be written in terms of the flux per unit solid angle or intensity $I_i(\theta, \phi)$ as:

$$\eta_i(\theta_{NA}) = \frac{\int_0^{2\pi} d\phi \int_0^{\theta_{NA}} d\theta I_i(\theta, \phi)}{\int_0^{2\pi} d\phi \int_0^{\pi} d\theta I_i(\theta, \phi)} \quad (5)$$

It is also useful to define the brightness enhancement, $\xi_i(\theta_{NA})$, as the ratio of the brightness of a dipole emitter into a certain NA to the brightness of a free dipole emitter into the same NA, i.e.:

$$\xi_i(\theta_{NA}) = \frac{\Phi_i(\theta_{NA})}{\Phi_{0i}(\theta_{NA})} = F_i^r \frac{\eta_i(\theta_{NA})}{\eta_{0i}(\theta_{NA})} \quad (6)$$

where $\eta_{0i}(\theta_{NA})$ refers to the collection efficiency of a free dipole.

The coupling of an emitter to an antenna has a few important consequences as shown in equations 3 and 4. Firstly, the quantum efficiency of the emitter or more generally the quantum efficiency of certain emission processes of the quantum emitter will be modified. For example it has been shown that coupling colloidal quantum dots with metal nanoparticles will increase the biexciton quantum efficiency [38]. This could be detrimental or beneficial depending on the application (e.g., single photon sources vs. bi-photon sources). The other two consequences are the modification of the emission pattern and decay rate which are the main focus of this paper.

3 Circular periodic ('Bullseye') nanoantenna with a central cavity

The structure studied in this section is based on our previous work in Refs [27, 28], as is shown schematically in figure 1c and d. It consists of a bullseye circular grating with 15 gratings, period Λ and a central cavity of radius R embedded in a dielectric layer of thickness h (realized by a polymer in [27, 28]). The emitter is considered as an oscillating dipole at the center of the circular grating and at height d from the metallic slab.

The large central cavity in the current antenna is introduced since we previously found that the presence of metallic corrugation near the emitter leads to efficient excitation of surface plasmons on the metal-dielectric interface which then results in a noticeable broadband random emission of photons, resulting not from the quantum emitter itself but rather from these surface plasmons. This excess random emission degraded the performance of a single photon device [27].

The operation mechanism of this system is as follows: When a quantum emitter (having a spectral band around the central emission wavelength λ_0) at

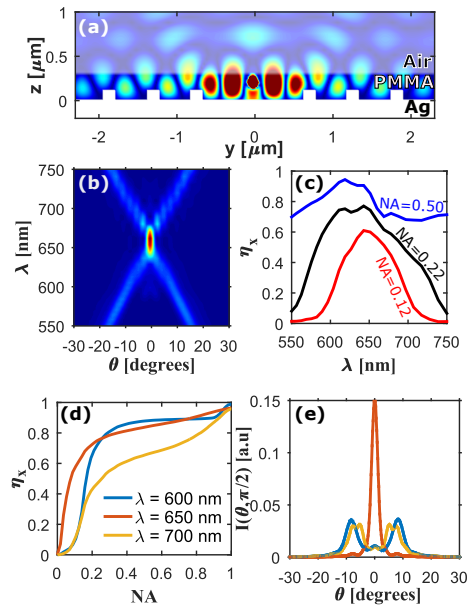


Figure 2: 3D Lumerical[®] simulation of the Bullseye Nanoantenna. (a) Electric field distribution due to a dipole emitter oriented along the x axis taken in the yz plane. (b) Angular emission spectrum $I(\theta, \lambda)$ for $\phi = \pi/2$ (yz-plane). (c) Collection efficiency into different NA's vs wavelength displaying the broadband response of the system. Collection efficiency (c) and angular intensity distribution for $\phi = \pi/2$ (d) for an emitter on resonance $\lambda = 650\text{nm}$ (red), and detuned from the antenna resonance $\lambda = 600\text{nm}$ (blue) and $\lambda = 700\text{nm}$ (yellow).

the center of the bullseye structure is excited it emits photons preferentially into the dielectric layer due to the higher index of refraction. The dielectric layer is designed to have modes that support this band of wavelengths (see supplementary information A) with corresponding propagation constants $\beta(\lambda)$. As the photons propagate in the radial direction they encounter a diffraction grating with period Λ that is designed to match the propagation constant ($\beta \approx 2\pi/\Lambda$) which diffracts the light. The diffracted photons that hit the air-dielectric surface with angles less than the critical angle couple out while all other photons continue to the next grating. Eventually nearly all the light is diffracted into free space modes and the interference between the various diffracted beams leads to a low divergence beam in the far field.

In addition to the geometric parameters of the antenna, the dipole orientation has a profound role in the performance of the device. Due to the azimuthal symmetry of the antenna we only need to consider two independent dipole orientations, the in-plane dipole (P_x) which will be represented by a dipole along the x axis (see figure 1b) and the out of plane dipole (P_z). Since the P_z dipole has a polarization that is predominantly in the z direction, it will mostly couple to the

z component of the TM_0 electric field for the metal-dielectric-air (MDA) slab waveguide (see supplementary information A). The electric field of this component is maximum near the metal surface and thus coupling into this mode requires either thicker dielectric layers which introduces higher order modes, or placing the dipole closer to the metal where diffraction is limited to the first few gratings thus lowering the redirection effect caused by constructive interference. On the other hand the P_x dipole couples into the TE_0 and the x-component of the TM_0 mode which both have field maxima near the center of the dielectric layer. This leads to better constructive interference into lower angles due to the diffraction caused by multiple circular grooves. It is clear from this discussion and from our simulations that the emission from the P_x dipole will have a better coupling with the antenna and thus better directionality. Moreover due to azimuthal symmetry an unpolarized source will have a probability of 2/3 to emit from an in-plane dipole (see supplementary information B). For these reasons we have chosen to optimize the structure considered in this section for the P_x dipole.

The performance of the device will be contingent on the geometrical parameters of the nanoantenna (see figure 1d) and the dipole orientation. Hence an optimization for these parameters for the P_x dipole was conducted using a particle swarm algorithm [34] in a 3D FDTD Lumerical[®] simulation [33]. The figure of merit for this optimization procedure was the system's brightness, i.e., its total flux, into an $NA = 0.22$ ($\Phi_x(0.22)$) in equation 4, corresponding to a typical NA of multimode fiber. The total flux was chosen rather than the collection efficiency to incorporate the radiative enhancement factor. The parameters are all normalized to the central wavelength of the source (λ_0) since the optimization shows that the structure scales well with wavelength in the spectral range between 600 and 800 nm (see supplementary information C). The dipole emitter was chosen to have a central wavelength of $\lambda_0 = 650$ nm. The optical parameters of the dielectric layer was chosen to match that of PMMA (Polymethyl methacrylate) which is optically transparent in the desired spectral range and is used for standard fabrication procedures [28].

The optimized structure described in this section has a normalized central radius $R/\lambda_0 = 0.97$, normalized grating period $\Lambda/\lambda_0 = 0.86$, normalized dielectric layer thickness $h/\lambda_0 = 0.41$, and normalized dipole height $d/\lambda_0 = 0.29$. The normalized ring width and height were set to 0.25 and 0.15 respectively.

From the simulations we can visualize both the near-field and far-field distributions. Figure 2a displays the simulated electric field inside the optimized structure in the plane normal to the dipole orientation (yz -plane). In this plane the emission couples into the TE_0 mode of the waveguide and we can observe that the standing waveguide modes have effective wavelengths that match the periodicity of the gratings. In the air layer above, the fields propagating out of the structure are visible. These fields have phases resulting in constructive interference in the far field into a narrow cone about $\theta = 0$. The far field spectral response of the antenna for wavelengths around the resonance wavelength ($\lambda = 650$ nm) is displayed in figure 2b. This far-field spectral intensity distribution ($I(\theta, \lambda)$) is plotted for the yz -plane ($\phi = 0$). Angular cross sections for

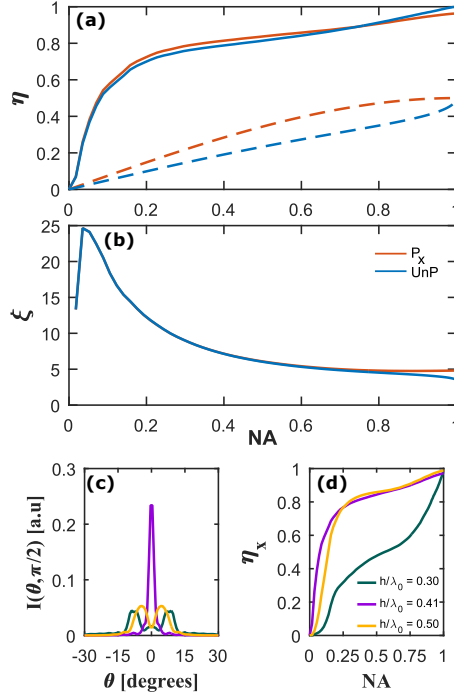


Figure 3: Collection efficiency (a) and brightness enhancement (b) for a dipole oriented along the x axis (P_x) and for a dipole emitting in a random orientation (UnP). The solid lines represent dipoles coupled to the antenna and the dashed lines represent dipoles in free space. Angular intensity distribution (c) and collection efficiency (d) for the optimized polymer thickness ($h/\lambda_0 = 0.41$) and for a thinner ($h/\lambda_0 = 0.3$) and thicker ($h/\lambda_0 = 0.5$) waveguide thickness.

the resonance wavelength ($\lambda = 650$ nm) and two detuned wavelengths ($\lambda = 600$ and 700 nm) are plotted in figure 2e. From these figures we can clearly see the dispersion resulting from the circular grating as the first orders (± 1) combine around $\lambda = 650$ nm to form a narrow directional beam. To better quantify the directionality of the emission the collection efficiency (defined in equation 5) for the same three wavelengths is shown in figure 2d. In figure 2c the collection efficiency as a function of wavelength is displayed for three collection NA's (0.12,0.22,0.50) corresponding to the NA of a single mode fiber and two commercially available multimode fibers respectively. From this figure and the overlap of the modes in figure 2b it is evident that the antenna's response is broadband (> 20 nm) which is beneficial for coupling to a room-temperature emitter. It is clear that detuning the emitter's wavelength from the designed wavelength will result in a lower collection efficiency at low NA corresponding to the formation of sidebands as seen in figure 2e.

Next we turn our attention to evaluating the performance of the device in

general and in particular to the dependence on dipole orientation. Due to the low-loss of the device we will be interested in the collection efficiency (equation 5) and brightness enhancement (equation 6). In this convention the radiative enhancement factor F_i^r is just $\xi_i(\pi)/2$. The collection efficiency and the brightness enhancement for a dipole oriented along the x-axis (P_x) and for an unpolarized dipole (UnP) are displayed in figure 3a and b respectively. These are compared to the corresponding values for free dipoles (dashed curves). The brightness for the unpolarized emitter is calculated from the two polarized ones, P_x and P_z (not shown here) as discussed in the supplementary information B. Using this brightness one can directly calculate the collection efficiency.

One very promising result is that around 74% of the emission of both the P_x and unpolarized emitters is collected already into a low, multi-mode fiber compatible numerical aperture of $NA = 0.22$, and an even higher collection efficiency of 82% is found for $NA = 0.5$, corresponding to a larger NA commercially available multi-mode fiber. This high coupling efficiencies into such low NA 's should enable direct coupling of the emission into a commercial multimode fiber. Moreover, as a result the confinement introduced by the antenna there is a net radiative enhancement of 2.4 and 1.7 for the P_x and unpolarized emitters respectively, which together with the improved collection, results in a brightness enhancement (figure 3b) of 11 (6) into the corresponding NA 's compared to that of a free standing dipole. This means a large increase in the usable photon rate from the source. It is visible that the brightness enhancement is especially high for low NA 's which is understandable due to the poor collection efficiency from the free-standing dipoles at low collection angles. It is worth noting that the brightness enhancement of the P_x and unpolarized dipoles overlap completely for nearly all the collection angles.

Another important point is the near identical collection efficiency curve of the P_x and unpolarized dipoles. This is due to the enhancement of the emission of P_x dipole and suppression of the P_z dipole so that the unpolarized dipole emission will result primarily from an in-plane dipole especially for low collection angles. This has the profound effect of transforming an emitter that originally emitted from all dipole orientations to an emitter that primarily emits from a dipole in a plane perpendicular to the nanoantenna. There is however, a probability of 1/3 to emit from a P_z dipole during each excitation cycle and the longer lifetime of this transition will result in a less time-deterministic source. Therefore it is advantageous to use a source that is originally polarized and whose dipole can be oriented in the plane of the nanoantenna. Such a source will enable the full use of all the benefits of this design while maintaining the deterministic nature of the source. One interesting candidate is the colloidal quantum rod reported by Sitt et al. [39]. In these quantum rods the symmetry is broken by using elongated shells (dot in rod) or elongated cores and shells (rod in rod) and the preferred transition has a dipole moment along the long axis of the quantum rod yielding degrees of polarization reaching 83%. [40, 41]. When spin-coated, the rods align in plane making them ideal for implementation in this new antenna design. Recently there has also been some significant progress in controlling the orientation of the emission dipole in NV centers in diamond

during chemical vapor deposition growth [42], which can also make them suitable for the proposed scheme.

Finally, we address the effect of varying the thickness of the waveguide layer. The angular intensity distribution and the collection efficiency for three thicknesses namely $h/\lambda_0 = 0.3, 0.41$, and 0.5 are shown in figure 3c and d respectively. Slightly changing the waveguide thickness will change the propagation constant of the fundamental TE_0 and TM_0 modes. Increasing the thickness further will result in the contribution of higher order modes (see Supplementary Information A) The former is the cause for the ranges of thicknesses in figure 3 c and d. The mismatch between the propagation constant and the grating Bragg wavevector leads to the formation of sidebands. The effect of the other geometrical parameters are discussed in the supplementary information section C.

One particularly interesting implementation (and perhaps test) of such designs is for single shot readout of spin-states in nitrogen vacancy centers in diamond. It was theoretically established that moderate Purcell factors might lead to a significantly enhanced SNR. [30]. As shown above such moderate Purcell factors can be realized. In fact, it is expected that for diamond waveguides the Purcell factor will be higher than reported above due to the higher index of refraction which leads to tighter confinement. This is confirmed by initial calculations (not shown here) where radiative enhancement factors as high as 8 were achieved. Furthermore, the SNR of the readout of the spin-state also benefits from efficient collection of the emitted photons, which is an added advantage of this design

It should be noted that the fabrication and analysis of bullseye structures around single NV centers has recently been reported with purely dielectric bullseye structure. [43] The predicted collection efficiency however was only 13% into an $NA = 0.7$. Other advances in the fabrication of photonic and plasmonic structures in diamond have been recently reported such as plasmonic apertures [44] and periodic nanocrystal arrays [45]. Silicon vacancies also provide for an interesting application particularly due to their near lifetime limited linewidths [46, 47]. Therefore implementing this design will open up an opportunity towards a highly efficient source of indistinguishable single photons necessary for quantum logic gates [31]

4 Composite Bullseye-nanocone nanoantenna

As discussed before, in addition to high collection efficiency, it is desirable to enhance the decay rate of a quantum emitter. The design of the previous section had a rather small increase of the intrinsic radiative rate of the emitter, due to the poor confinement of the optical mode around the dipole, and the low LDOS of the essentially dielectric waveguide mode. To overcome this intrinsic limitation, we have considered introducing a plasmonic structure at the center of the bullseye nanoantenna. An interesting candidate is the silver or gold nanocone. These nanocones have a longitudinal mode along the cone's axis and a transverse mode along the base. [48] The longitudinal mode in particular

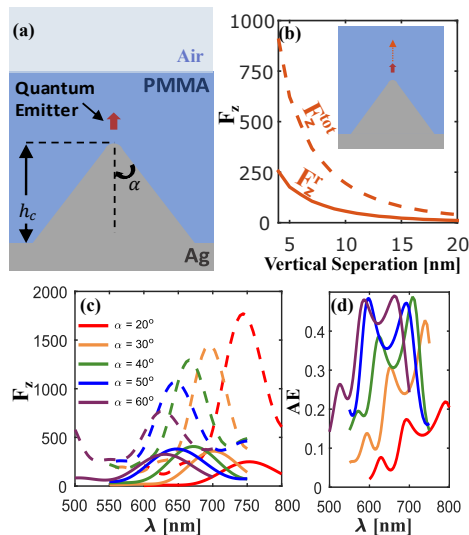


Figure 4: (a) Schematic for the a silver nanocone with rounded tip embedded in a dielectric layer. (b) Radiative (solid) and total (dashed) enhancement factor as a function of vertical separation between the dipole and nanocone with $\alpha = 50^\circ$. (c) Radiative (solid) and total (dashed) decay rate enhancement for nanocones of different apex angles. (d) Antenna quantum efficiency for nanocones of different apex angles

offers high field enhancement due the lightning rod effect near the rod's tip. [49] Recent theoretical studies on silver nanocones showed that the plasmonic resonance can be tuned across the optical spectrum by changing the apex angle of the cone. [50, 51, 52] Furthermore the study demonstrated that the largest quantum yields occur for larger nanocones of heights around 160 nm and angles of $\pi/6$ [50]. A similar theoretical study on gold nanocones also displayed the shift of the plasmonic resonance with tip angle at fixed cone heights. [53] A detailed study of the electric field enhancement of these nanocones and their dependence on the cone parameters can be found in, e.g., [54, 55, 51, 52]

The difficulty of using nanocones for emission rate enhancement presides in the fact that the emitter must be placed with sub 10 nm precision near the tip of the nanocone. Furthermore, the vertical separation between the emitter and the tip needs to be of the order of a few nanometers due to the high localization of the field. Recently both problems were addressed by chemically binding NQDs preferentially to the tip of gold nanocones .[56] The molecular binding and the shell of the NQD provided a vertical separation of around 4 nm. [56].

Since we are interested in exciting the longitudinal mode of the nanocone a dipole oriented along the z-axis is considered in this section. First we consider a nanocone of height h_c and apex angle α on a metal slab embedded in a dielectric (PMMA) layer without the presence of the bullseye rings (see figure

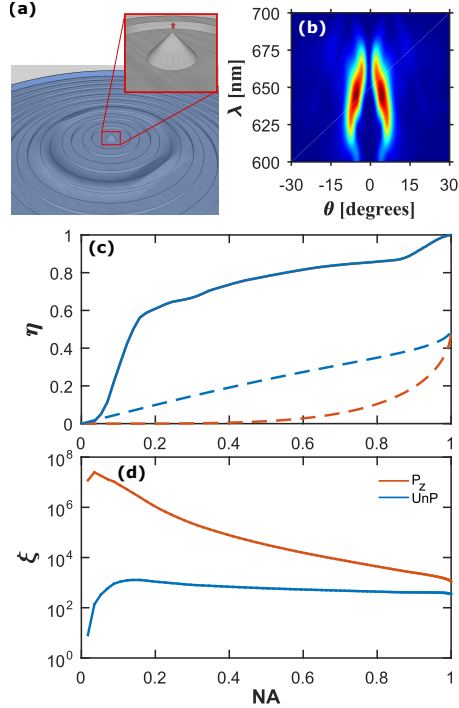


Figure 5: (a) Schematic for the a silver nanocone embedded in a bullseye nanoantenna. (b) Angular intensity spectrum $I(\theta, \lambda)$ for a dipole emitter ($\lambda_0 = 650$ nm) in a composite bullseye nanocone antenna. Collection efficiency (c) and brightness enhancement (d) of a dipole emitter in the optimized composite structure for the vertical dipole (P_z) and unpolarized dipole (UnP). The dashed lines represent the values for dipoles in free space

4a). We vary the cone apex angle (α) and dipole ($\lambda_0 = 650$ nm) location in the vertical direction while keeping the PMMA thickness ($h = 620$ nm) and cone height ($h_c = 170$ nm) fixed as in the optimized structure discussed later. (figure 4b-d) It can be seen from figure 4b that locating the dipole within a few nanometers from the cone tip is essential in achieving high enhancement factors. The dipole height is fixed at 4 nm due to fabrication limitations in subsequent calculations. Figure 4c displays the redshift of the longitudinal plasmonic resonance as the apex angle is reduced as discussed above. An important aspect is that the enhancements are broadband with FWHM ~ 80 nm which is essential for broadband room-temperature emitters and fits well with the the broadband emission redirection offered by the bullseye nanoantenna. Furthermore we find that the antenna quantum efficiency is best for larger nanocones as has been reported previously (figure 4d). [50, 53]

Next we place the nanocone at the center of the bullseye nanoantenna. A

close-up view of the structure is shown schematically in figure 5a with a zoom-in display of the nanocone in the inset. The different dipole orientation and effective dipole height force a new optimization for both collection efficiency and brightness enhancement factor. We thus use the same figure of merit as in section 3 which is the far-field brightness for an NA of 0.22 (i.e. $\Phi_z(0.22)$). The optimization is carried out for a dipole emitter at central wavelength $\lambda_0 = 650$ nm and which is oriented along the cone axis (P_z). The optimization clearly pushes towards thicker polymer layers and lower groove heights due to the preferential coupling of the nanocone-emitter sub-system into the *TM* modes of the waveguide layer as discussed in section 3. The parameters for the bullseye nanoantenna are: normalized central radius $R/\lambda_0 = 0.99$; normalized grating period $\Lambda/\lambda_0 = 0.86$; normalized polymer thickness $h/\lambda_0 = 0.95$; and normalized groove heights and widths equal to 0.167 and 0.500 respectively. A nanocone of height $h_c = 170$ nm and apex angle $\alpha = 50^\circ$ is placed at the center of the bullseye structure and the dipole emitter is located 4 nm above the tip of the nanocone. The far-field angular intensity distribution is displayed in figure 5b featuring a broad resonance and narrow angular emission pattern. At resonance ($\lambda = 650$ nm) the angular pattern has a prominent angular ring at an angle of $\sim 4.5^\circ$. As shown in figure 5c this pattern results in a collection efficiency into an $NA = 0.22$ (0.5) of around 61% (78%) respectively for both the P_z and unpolarized dipole orientations. Due to high enhancement of one dipole orientation over the other the flux of an unpolarized emitter acquires the dependency of the P_z dipole with an overall flux of about 1/3 that of the P_z dipole. Thus the collection efficiency of the unpolarized and P_z dipoles are essentially identical.

A brightness enhancement factor into these NA's are ~ 1000 (~ 600) for an unpolarized emitter (figure 5d). The extremely high brightness enhancement at low NA for the P_z dipole is due to the extremely poor collection efficiency of the corresponding free dipole (see figure 5c). Moreover the overall radiative enhancement factor is ~ 240 with an antenna efficiency of around 31%.

The implementation of this design will vary depending on the particular emitter in question. A particularly interesting application would be for NQDs since the ability to bond these nanocrystals to the tips of the nanocone has been developed. [56, 48] In particular, the biexciton quantum efficiency will be increased due to the low intrinsic quantum efficiency of the biexciton emission (see figure 1a and equation 3),[38], giving rise to a potential bi-photon source.

For sources where the single-photon purity is retained even when the decay rate is enhanced such as color centers in diamond, this design will permit the fabrication of a bright and efficient single photon source. Such a source will improve quantum key distribution systems which currently use faint laser pulses with an average photon number of $\langle n \rangle \approx 0.5$ per pulse. An ideal single photon source will have $\langle n \rangle \approx 1$ which requires both a high single photon purity and high collection efficiency (> 0.5) [31]. Furthermore the emission rate must be in the GHz regime to compete with the current technology which requires high radiative enhancement factors. Since SiV centers already have intrinsic lifetimes on the order of ~ 1 ns and display good single photon purities [47] it is not long shot to satisfy these requirements using the composite bullseye-

nanocone antenna. Small nanodiamonds containing SiV centers may be placed in the proximity of the nanocone by a scanning probe tip using a pick and place technique [57].

5 Conclusion

Our new design and FDTD calculations suggest an optimized bullseye nanoantenna with over 82% collection efficiency into an NA of a multimode fiber and a corresponding source brightness that is more than 10 fold that of a dipole of free space. We have also investigated a composite structure that combines both high collection efficiency ($\eta(NA = 0.22) = 0.61$) and high radiative enhancement ($\Gamma_z^r = 240$) using a silver nanocone at the center of a bullseye nanoantenna.

These results are especially promising for the production of a high-rate, room-temperature on-chip single photon sources that can be directly coupled to optical fibers without any additional optics. This structure can be also used for example along with color centers in diamond (e.g. SiV and NV centers) enabling applications spanning various fields including quantum communication and magnometric sensing [42]. It is important to emphasize that these structures are not limited to any specific quantum emitter and can be applied universally, limited only by challenges in fabrication.

Acknowledgements

This work is supported in parts by The Einstein Foundation Berlin; The U.S. Department of Energy: Office of Basic Energy Sciences, Division of Materials Sciences and Engineering; The European Cooperation in Science and Technology through COST Action MP1302 Nanospectroscopy; The Ministry of Science and Technology, Israel.

References

- [1] Jeremy L. O'Brien, Akira Furusawa, and Jelena Vučković. Photonic quantum technologies. *Nature Photonics*, 3(12):687–695, 12 2009.
- [2] Jonathan P. Dowling and Gerard J. Milburn. Quantum technology: the second quantum revolution. *Philosophical Transactions of the Royal Society of London A: Mathematical, Physical and Engineering Sciences*, 361(1809), 2003.
- [3] Brahim Lounis and Michel Orrit. Single-photon sources. *Reports on Progress in Physics*, 68(5):1129–1179, 5 2005.
- [4] H. J. Kimble, M. Dagenais, and L. Mandel. Photon Antibunching in Resonance Fluorescence. *Physical Review Letters*, 39(11):691–695, 9 1977.

- [5] Franois Treussart, Andr Clouqueur, Carl Grossman, and Jean-Franois Roch. Photon antibunching in the fluorescence of a single dye molecule embedded in a thin polymer film. *Optics Letters*, 26(19):1504, 10 2001.
- [6] Elke Neu, Mario Agio, and Christoph Becher. Photophysics of single silicon vacancy centers in diamond: implications for single photon emission. *Optics Express*, 20(18):19956, 8 2012.
- [7] B. Lounis, H.A. Bechtel, D. Gerion, P. Alivisatos, and W.E. Moerner. Photon antibunching in single CdSe/ZnS quantum dot fluorescence. 2000.
- [8] Xing Ding, Yu He, Z.-C. Duan, Niels Gregersen, M.-C. Chen, S. Unsleber, S. Maier, Christian Schneider, Martin Kamp, Sven Höfling, Chao-Yang Lu, and Jian-Wei Pan. On-Demand Single Photons with High Extraction Efficiency and Near-Unity Indistinguishability from a Resonantly Driven Quantum Dot in a Micropillar. *Physical Review Letters*, 116(2):020401, 1 2016.
- [9] Swayandipta Dey and Jing Zhao. Plasmonic Effect on Exciton and Multiexciton Emission of Single Quantum Dots. *The Journal of Physical Chemistry Letters*, 7(15):2921–2929, 8 2016.
- [10] Matthew Pelton. Modified spontaneous emission in nanophotonic structures. *Nature Photonics*, 9(7):427–435, 6 2015.
- [11] R. Esteban, T. V. Teperik, and J. J. Greffet. Optical Patch Antennas for Single Photon Emission Using Surface Plasmon Resonances. *Physical Review Letters*, 104(2):026802, 1 2010.
- [12] C. Belacel, B. Habert, F. Bigourdan, F. Marquier, J.-P. Hugonin, S. Michaelis de Vasconcellos, X. Lafosse, L. Coolen, C. Schwob, C. Javaux, B. Dubertret, J.-J. Greffet, P. Senellart, and A. Maitre. Controlling Spontaneous Emission with Plasmonic Optical Patch Antennas. *Nano Letters*, 13(4):1516–1521, 4 2013.
- [13] F. Bigourdan, F. Marquier, J.-P. Hugonin, and J.-J. Greffet. Design of highly efficient metallo-dielectric patch antennas for single-photon emission. *Optics Express*, 22(3):2337, 2 2014.
- [14] Nitzan Livneh, Ayelet Strauss, Ilai Schwarz, Itamar Rosenberg, Adiel Zimran, Shira Yochelis, Gang Chen, Uri Banin, Yossi Paltiel, and Ronen Rapaport. Highly Directional Emission and Photon Beaming from Nanocrystal Quantum Dots Embedded in Metallic Nanoslit Arrays. *Nano Letters*, 11(4):1630–1635, 4 2011.
- [15] Alberto G. Curto, Giorgio Volpe, Tim H. Taminiau, Mark P. Kreuzer, Romain Quidant, and Niek F. van Hulst. Unidirectional Emission of a Quantum Dot Coupled to a Nanoantenna. *Science*, 329(5994), 2010.

- [16] Daniel Dregely, Richard Taubert, Jens Dorfmueller, Ralf Vogelgesang, Klaus Kern, Harald Giessen, A. Alù, N. Engheta, M. Brongersma, L. Novotny, P. Bharadwaj, B. Deutsch, L. Novotny, S. Kühn, P. Mühlischlegel, J. Dorfmueller, P. Schuck, R. Esteban, T. V. Teperik, J. J. Greffet, T. H. Taminiau, F. D. Stefani, N. F. van Hulst, H. F. Hofmann, T. Kosako, Y. Kadoya, J. Li, A. Salandrino, N. Engheta, A. F. Koenderink, J. R. Carson, T. Taminiau, T. Pakizeh, M. Käll, H. Yagi, T. Kosako, Y. Kadoya, H. F. Hofmann, A. G. Curto, N. Liu, J. Dorfmueller, C. Middlebrook, J. Huang, A. Alù, N. Engheta, P. Johnson, and R. Christy. 3D optical YagiUda nanoantenna array. *Nature Communications*, 2:267, 4 2011.
- [17] Haibo Li, Shuping Xu, Yuejiao Gu, Hailong Wang, Renping Ma, John R. Lombardi, and Weiqing Xu. Active Plasmonic Nanoantennas for Controlling Fluorescence Beams. *The Journal of Physical Chemistry C*, 117(37):19154–19159, 9 2013.
- [18] Moshe G. Harats, Nitzan Livneh, Gary Zaiats, Shira Yochelis, Yossi Paltiel, Efrat Lifshitz, and Ronen Rapaport. Full Spectral and Angular Characterization of Highly Directional Emission from Nanocrystal Quantum Dots Positioned on Circular Plasmonic Lenses. *Nano Letters*, 14(10):5766–5771, 10 2014.
- [19] Vincenzo Giannini, Antonio I. Fernandez-Dominguez, Susannah C. Heck, and Stefan A. Maier. Plasmonic Nanoantennas: Fundamentals and Their Use in Controlling the Radiative Properties of Nanoemitters. *Chemical Reviews*, 111(6):3888–3912, 6 2011.
- [20] Dirk Englund, Ilya Fushman, Andrei Faraon, and Jelena Vučković. Quantum dots in photonic crystals: From quantum information processing to single photon nonlinear optics. *Photonics and Nanostructures - Fundamentals and Applications*, 7(1):56–62, 2009.
- [21] A. Laucht, T. Günthner, S. Pütz, R. Saive, S. Frédérick, N. Hauke, M. Bichler, M.-C. Amann, A. W. Holleitner, M. Kaniber, and J. J. Finley. Broadband Purcell enhanced emission dynamics of quantum dots in linear photonic crystal waveguides. *Journal of Applied Physics*, 112(9):093520, 11 2012.
- [22] V. S. C. Manga Rao and S. Hughes. Single quantum-dot Purcell factor and β factor in a photonic crystal waveguide. *Physical Review B*, 75(20):205437, 5 2007.
- [23] S. Ates, S. M. Ulrich, S. Reitzenstein, A. Löffler, A. Forchel, and P. Michler. Post-Selected Indistinguishable Photons from the Resonance Fluorescence of a Single Quantum Dot in a Microcavity. *Physical Review Letters*, 103(16):1–4, 2009.
- [24] M. Davanço, M. T. Rakher, D. Schuh, A. Badolato, and K. Srinivasan. A circular dielectric grating for vertical extraction of single quantum dot emission. *Applied Physics Letters*, 99(4):041102, 7 2011.

- [25] Alexander Krasnok, Stanislav Glybovski, Mihail Petrov, Sergey Makarov, Roman Savelev, Pavel Belov, Constantin Simovski, and Yuri Kivshar. Demonstration of the enhanced Purcell factor in all-dielectric structures. *Applied Physics Letters*, 108(21):211105, 5 2016.
- [26] Nitzan Livneh, Moshe G. Harats, Shira Yochelis, Yossi Paltiel, and Ronen Rapaport. Efficient Collection of Light from Colloidal Quantum Dots with a Hybrid MetalDielectric Nanoantenna. *ACS Photonics*, 2(12):1669–1674, 12 2015.
- [27] Nitzan Livneh, Moshe G. Harats, Daniel Istrati, Hagai S. Eisenberg, and Ronen Rapaport. Highly Directional Room-Temperature Single Photon Device. *Nano Letters*, 16(4):2527–2532, 2016.
- [28] Moshe G. Harats, Nitzan Livneh, and Ronen Rapaport. Design, fabrication and characterization of a hybrid metal-dielectric nanoantenna with a single nanocrystal for directional single photon emission. *Optical Materials Express*, 7(3):834, 3 2017.
- [29] J.G. Rarity, P.C.M. Owens, and P.R. Tapster. Quantum Random-number Generation and Key Sharing. *Journal of Modern Optics*, 41(12):2435–2444, 12 1994.
- [30] S. A. Wolf, I. Rosenberg, R. Rapaport, and N. Bar-Gill. Purcell-enhanced optical spin readout of nitrogen-vacancy centers in diamond. *Physical Review B*, 92(23):235410, 12 2015.
- [31] Igor Aharonovich, Dirk Englund, and Milos Toth. Solid-state single-photon emitters. *Nature Photonics*, 10(10):631–641, 9 2016.
- [32] Allen. Taflove and Susan C. Hagness. *Computational electrodynamics : the finite-difference time-domain method*. Artech House, 2005.
- [33] Lumerical Solutions, Inc.
- [34] J. Robinson and Y. Rahmat-Samii. Particle Swarm Optimization in Electromagnetics. *IEEE Transactions on Antennas and Propagation*, 52(2):397–407, 2 2004.
- [35] Amardeep M. Jagtap, Jayakrishna Khatei, K. S. R. Koteswara Rao, B. Hennequin, N. R. Thomas, D. J. Binks, A. Eychmüller, Y. Masumoto, M. Lomascolo, P. Frigeri, S. Franchi, C. H. A. Huan, Y. P. Feng, and Q. Xiong. Excitonphonon scattering and nonradiative relaxation of excited carriers in hydrothermally synthesized CdTe quantum dots. *Phys. Chem. Chem. Phys.*, 17(41):27579–27587, 2015.
- [36] Istvn Robel, Ryan Gresback, Uwe Kortshagen, Richard D. Schaller, and Victor I. Klimov. Universal Size-Dependent Trend in Auger Recombination in Direct-Gap and Indirect-Gap Semiconductor Nanocrystals. *Physical Review Letters*, 102(17):177404, 5 2009.

- [37] Purcell. Spontaneous emission probabilities at radio frequencies. *Physical Review*, 69, 1946.
- [38] Korenobu Matsuzaki, Simon Vassant, Hsuan-Wei Liu, Anke Dutschke, Bjrn Hoffmann, Xuewen Chen, Silke Christiansen, Matthew R. Buck, Jennifer A. Hollingsworth, Stephan Götzinger, and Vahid Sandoghdar. Strong plasmonic enhancement of biexciton emission: controlled coupling of a single quantum dot to a gold nanocone antenna. *Scientific Reports*, 7:42307, 2 2017.
- [39] Amit Sitt, Asaf Salant, Gabi Menagen, and Uri Banin. Highly Emissive Nano Rod-in-Rod Heterostructures with Strong Linear Polarization. *Nano Letters*, 11(5):2054–2060, 5 2011.
- [40] Ido Hadar, Gal B. Hitin, Amit Sitt, Adam Faust, and Uri Banin. Polarization properties of semiconductor nanorod heterostructures: From single particles to the ensemble. *Journal of Physical Chemistry Letters*, 4(3):502–507, 2013.
- [41] Amit Sitt. *Size and Dimensionality Effects on Optical Properties of Heterostructured Semiconductor Nanocrystals*. PhD thesis, The Hebrew University of Jerusalem, 2012.
- [42] Tim Schröder, Sara L. Mouradian, Jiabao Zheng, Matthew E. Trusheim, Michael Walsh, Edward H. Chen, Luozhou Li, Igal Bayn, and Dirk Englund. Quantum nanophotonics in diamond [Invited]. *Journal of the Optical Society of America B*, 33(4):B65, 4 2016.
- [43] Luozhou Li, Edward H. Chen, Jiabao Zheng, Sara L. Mouradian, Florian Dolde, Tim Schröder, Sinan Karaveli, Matthew L. Markham, Daniel J. Twitchen, and Dirk Englund. Efficient Photon Collection from a Nitrogen Vacancy Center in a Circular Bullseye Grating. *Nano Letters*, 15(3):1493–1497, 3 2015.
- [44] JT Choy, BJM Hausmann, TM Babinec, and I Bulu. Enhanced single-photon emission from a diamond-silver aperture. *Nature*, 2011.
- [45] Igor Aharonovich, Jonathan C. Lee, Andrew P. Magyar, David O. Bracher, and Evelyn L. Hu. Bottom-up engineering of diamond micro- and nanostructures. *Laser & Photonics Reviews*, 7(5):L61–L65, 9 2013.
- [46] A. Sipahigil, K.D. Jahnke, L.J. Rogers, T. Teraji, J. Isoya, A.S. Zibrov, F. Jelezko, and M.D. Lukin. Indistinguishable Photons from Separated Silicon-Vacancy Centers in Diamond. *Physical Review Letters*, 113(11):113602, 9 2014.
- [47] Ke Li, Yu Zhou, A. Rasmita, I. Aharonovich, and W.B. Gao. Nonblinking Emitters with Nearly Lifetime-Limited Linewidths in CVD Nanodiamonds. *Physical Review Applied*, 6(2):024010, 8 2016.

- [48] Alfred J. Meixner, Regina Jäger, Sebastian Jäger, Annika Bräuer, Kerstin Scherzinger, Julia Fulmes, Sven zur Oven Krockhaus, Dominik A. Gollmer, Dieter P. Kern, and Monika Fleischer. Coupling single quantum dots to plasmonic nanocones: optical properties. *Faraday Discuss.*, 184(0):321–337, 2015.
- [49] M. Fleischer, C. Stanciu, F. Stade, J. Stadler, K. Braun, A. Heeren, M. Häffner, D. P. Kern, and A. J. Meixner. Three-dimensional optical antennas: Nanocones in an apertureless scanning near-field microscope. *Applied Physics Letters*, 93(11):111114, 9 2008.
- [50] Stefania DAgostino, Fabio Della Sala, and Lucio Claudio Andreani. Dipole Decay Rates Engineering via Silver Nanocones. *Plasmonics*, 8(2):1079–1086, 6 2013.
- [51] A. V. Goncharenko, M. M. Dvoynenko, Hung-Chih Chang, and Juen-Kai Wang. Electric field enhancement by a nanometer-scaled conical metal tip in the context of scattering-type near-field optical microscopy. *Applied Physics Letters*, 88(10):104101, 3 2006.
- [52] A.V. Goncharenko, Hung-Chih Chang, and Juen-Kai Wang. Electric near-field enhancing properties of a finite-size metal conical nano-tip. *Ultramicroscopy*, 107(2):151–157, 2007.
- [53] Ahmad Mohammadi, Franziska Kaminski, Vahid Sandoghdar, and Mario Agio. Fluorescence Enhancement with the Optical (Bi-) Conical Antenna. *The Journal of Physical Chemistry C*, 114(16):7372–7377, 4 2010.
- [54] Yves C. Martin, Hendrik F. Hamann, and H. Kumar Wickramasinghe. Strength of the electric field in apertureless near-field optical microscopy. *Journal of Applied Physics*, 89(10):5774–5778, 5 2001.
- [55] Anatoliy V Goncharenko, Juen-Kai Wang, and Yia-Chung Chang. Electric near-field enhancement of a sharp semi-infinite conical probe: Material and cone angle dependence.
- [56] Julia Fulmes, Regina Jäger, Annika Bräuer, Christian Schäfer, Sebastian Jäger, Dominik A. Gollmer, Andreas Horrer, Elke Nadler, Thomas Chassé, Dai Zhang, Alfred J. Meixner, Dieter P. Kern, and Monika Fleischer. Self-aligned placement and detection of quantum dots on the tips of individual conical plasmonic nanostructures. *Nanoscale*, 7(35):14691–14696, 2015.
- [57] Andreas W. Schell, Gnter Kewes, Tim Schröder, Janik Wolters, Thomas Aichele, and Oliver Benson. A scanning probe-based pick-and-place procedure for assembly of integrated quantum optical hybrid devices. *Review of Scientific Instruments*, 82(7):073709, 7 2011.

Supplementary Information

Quantum emitters coupled to circular nanoantennas for high brightness quantum light sources

Hamza A. Abudayyeh¹ and Ronen Rapaport^{1,2}

¹ Racah Institute for Physics, and ² the Applied Physics Department, The Hebrew University of Jerusalem, Jerusalem 9190401, Israel

A Modes of metal dielectric air (MDA) waveguide

The system considered here is shown in figure S1. This structure is a special form of the three layer waveguide structure with the substrate as a perfect electric conductor and the cladding is air. The solutions of the wave equations that we are interesting in are those that result in a propagating waveguide mode (i.e. in the x direction). It is also assumed that the waveguide is homogeneous in the y-direction. Therefore the spatial dependence of the electromagnetic fields will have the following form:

$$\begin{aligned}\vec{E}(x, y, z) &= \vec{e}(z) \exp(i\beta x) \\ \vec{H}(x, y, z) &= \vec{h}(z) \exp(i\beta x)\end{aligned}\tag{S1}$$

Substituting equations S1 into Maxwell's equations results in two sets of solutions for the transverse electric (TE) and transverse magnetic (TM) polarizations.

TE polarization

For this polarization the nonzero field components are e_y , h_x and h_z . Since we are looking for propagating modes in the waveguide we assume that the fields are evanescent in the air layer. Furthermore the parallel electric field must vanish at the PEC surface. Thus it is clear that the solutions must take the form of:

$$e_y(z) = \begin{cases} A \sin(\kappa z), & 0 \leq z \leq h \\ B \exp(-\gamma(z-h)), & z \geq h \end{cases}\tag{S2}$$

Assuming harmonic time dependence, κ and γ must satisfy :

$$\begin{aligned}\beta^2 + \kappa^2 &= \frac{n^2 \omega^2}{c^2} \\ \beta^2 - \gamma^2 &= \frac{\omega^2}{c^2}\end{aligned}\tag{S3}$$

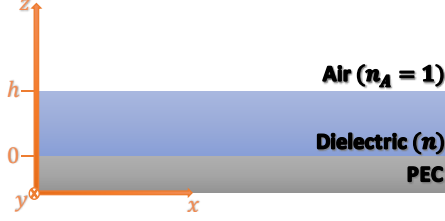


Figure S1: Diagram of metal dielectric air waveguide.

The parallel electric and magnetic fields need to be continuous at the dielectric air boundary which results in the following equations:

$$\begin{aligned} A \sin(\kappa h) &= B \\ A \kappa \cos(\kappa h) &= -\gamma B \end{aligned} \quad (S4)$$

By dividing these equations we reach to the following transcendental equation:

$$\tan(\kappa h) = -\frac{\kappa}{\gamma} \quad (S5)$$

By solving equations S3 and S5 simultaneously one obtains the dispersion relation ($\omega(\beta)$). Clearly this would lead to an infinite number of modes each having a cutoff that occurs when the field is no longer confined to the waveguide layer (i.e. $\gamma \rightarrow 0$). Therefore the cutoff condition occurs when $\tan(\kappa h) = -\infty$. This can be written in terms of the free-space wavelength $\lambda_0 = 2\pi c/\omega$ and the waveguide thickness as:

$$\frac{h_{cutoff}^{(\nu)}}{\lambda_0} = \frac{2\nu + 1}{4\sqrt{n^2 - 1}} \quad (S6)$$

where $\nu = 0, 1, 2, \dots$ is the mode number and $h_{cutoff}^{(\nu)}$ is the minimum waveguide thickness that would support the TE_ν mode. The electric field of the TE_ν mode can therefore be given as:

$$E_y^{(\nu)}(x, z) = \begin{cases} E_0 \sin(\kappa_\nu z) \exp(i\beta_\nu x), & 0 \leq z \leq h \\ E_0 \sin(\kappa_\nu h) \exp(-\gamma_\nu(z-h)) \exp(i\beta_\nu x), & z \geq h \end{cases} \quad (S7)$$

, and the magnetic field may be found by applying Maxwell's equations.

TM polarization

For this polarization the non-vanishing fields are h_y , e_x , and e_z . Therefore it is easier to solve the equations in terms of the magnetic field h_y and then apply Maxwell's curl equations to find the electric field components. As before we assume a confined propagating field which leads to the ansatz:

$$h_y(z) = \begin{cases} A \cos(\kappa z), & 0 \leq z \leq h \\ B \exp(-\gamma(z-h)), & z \geq h \end{cases} \quad (S8)$$

where the cosine was chosen to force the tangential electric field (e_x) to vanish at the conductor surface. The parameters κ and γ are still related to the propagation constant β by equation S3. By applying the continuity of the tangential electric and magnetic fields at the dielectric air interface we reach to the following conditions:

$$\begin{aligned} A \cos(\kappa h) &= B \\ \frac{A}{n^2} \kappa \sin(\kappa h) &= \gamma B \end{aligned} \quad (\text{S9})$$

which yields the transcendental equation:

$$\tan(\kappa h) = \frac{n^2 \gamma}{\kappa} \quad (\text{S10})$$

Again a mode is cutoff when $\gamma \rightarrow 0$, or $\tan(\kappa h) = 0$. This yields the following condition:

$$\frac{h_{cutoff}^{(\nu)}}{\lambda_0} = \frac{\nu}{2\sqrt{n^2 - 1}} \quad (\text{S11})$$

with $\nu = 0, 1, 2, \dots$ corresponds to the TM_ν mode. One important difference is that the TM_0 mode has no cutoff and therefore is always present regardless of the thickness or wavelength considered.

We can get the electric field components by applying the curl equations to obtain:

$$\begin{aligned} E_z^{(\nu)}(x, z) &= \begin{cases} E_0 \sin(\kappa_\nu z) \exp(i\beta_\nu x), & 0 \leq z \leq h \\ E_0 \sin(\kappa_\nu h) \exp(-\gamma_\nu(z-h)) \exp(i\beta_\nu x), & z \geq h \end{cases} \\ E_x^{(\nu)}(x, z) &= \begin{cases} \frac{-iE_0 \beta_\nu}{\kappa_\nu} \cos(\kappa_\nu z) \exp(i\beta_\nu x), & 0 \leq z < h \\ \frac{iE_0 \beta_\nu}{\kappa_\nu} \sin(\kappa_\nu h) \exp(-\gamma_\nu(z-h)) \exp(i\beta_\nu x), & z > h \end{cases} \end{aligned} \quad (\text{S12})$$

B Incoherent unpolarized dipole sources

Here we will discuss how the fields and flux of an unpolarized dipole source may be calculated. The field by an unpolarized source may be calculated by an incoherent superposition of the fields of randomly oriented oscillating dipoles, i.e.:

$$\langle |\Psi|^2 \rangle = \frac{1}{4\pi} \int \int |\Psi(\theta', \phi')|^2 \sin(\theta') d\theta' d\phi' \quad (\text{S13})$$

where Ψ is a general vector field that can represent the electric or magnetic field and $\langle \dots \rangle$ signifies an average over all dipole orientations. θ' and ϕ' are the polar and azimuthal angles of the dipole and are not to be confused with the polar and azimuthal angles of the position vector $\vec{r}'(\theta, \phi)$. It is worth noting that all the fields in this section have implicit dependence on \vec{r}' which we dropped from the notation. Such a randomly oriented dipole can in general be decomposed into three orthogonal dipoles \vec{P}_x , \vec{P}_y , and \vec{P}_z oriented along the axes of some coordinate system as follows:

$$\vec{P} = \vec{P}_x \sin(\theta') \cos(\phi') + \vec{P}_y \sin(\theta') \sin(\phi') + \vec{P}_z \cos(\theta') \quad (\text{S14})$$

We can therefore write the field of an unpolarized source as:

$$\vec{\Psi}(\theta', \phi') = \vec{\Psi}_x \sin(\theta') \cos(\phi') + \vec{\Psi}_y \sin(\theta') \sin(\phi') + \vec{\Psi}_z \cos(\theta') \quad (\text{S15})$$

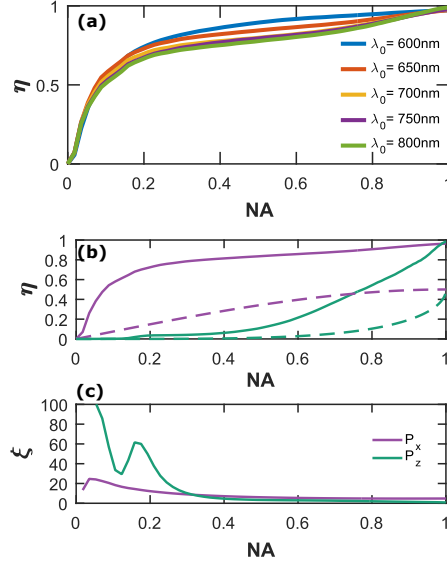


Figure S2: (a) Collection efficiency for the structure scaled to different central wavelengths. Collection efficiency (η) (b) and Brightness enhancement (ξ) (c) for the optimized structure for dipoles oriented along the x and z axes (solid curves) . The dashed lines represent the curves for dipoles in free space.

where $\vec{\Psi}_i$ represents the field due to the dipole \vec{P}_i . Substituting equation S15 into equation S13 and using some integral identities gives the following relation:

$$\langle |\Psi|^2 \rangle = \frac{1}{3} (|\Psi_x|^2 + |\Psi_y|^2 + |\Psi_z|^2) \quad (\text{S16})$$

This derivation assumes that the orientation of the dipole is completely random i.e. P_i and thus Ψ_i have no dependence on θ' or ϕ' . Equation S16 is equally valid for the electric and magnetic field and is therefore valid for the flux:

$$\langle F \rangle = \frac{1}{3} (F_x + F_y + F_z) \quad (\text{S17})$$

For a system with azimuthal symmetry this reduces to:

$$\langle F \rangle = \frac{2}{3} F_x + \frac{1}{3} F_z \quad (\text{S18})$$

C Circular periodic ('Bullseye') nanoantenna with a central cavity

In this section we show supplementary results for section 3 in the main text.

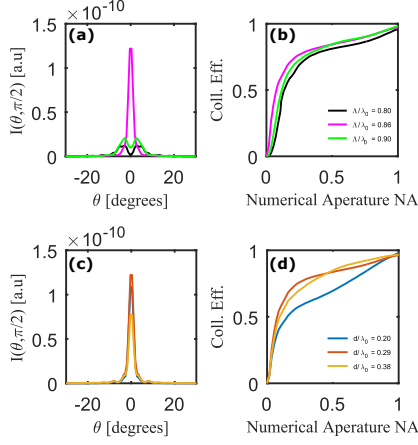


Figure S3: Intensity angular distribution in the yz -plane (a and c) and the collection efficiency (b and d) for various values of the period (a and b) and the dipole height (c and d).

Device geometrical parameters scalability with emitter wavelength:

One important feature that the design of the nanoantenna possesses is scalability of its geometrical parameters with the emitter's wavelength. For this reason we chose in the main text to normalize lengths to the emitter's central wavelength to make the reported parameters general for all relevant emission wavelengths. In order to display this we plot in figure S2a the collection efficiency for various central wavelengths between 600 and 800 nm where we scale the nanoantenna dimensions to the central wavelength. The figure clearly shows that the differences between the various central wavelengths is small and that the overall trend is the same for all wavelengths. The differences can be mainly attributed to the wavelength dispersion of the metal optical properties. The dispersion of the dielectric in the wavelength range considered can be neglected.

Device emission dependence on dipole orientation

We complement the discussion about the dipole orientation in the main text here by displaying the collection efficiency and brightness enhancement (defined in equations 6 and 7 in the main text) for the P_z dipole in figure S2b and c respectively. As compared to the P_x orientation the P_z dipole is both suppressed ($F_z^r \approx 0.45$) and the collection efficiency is low for low numerical apertures. This emphasizes the point made in the main text that an unpolarized emitter will emit preferentially with a dipole oriented along the x -axis especially at low NA.

Device emission dependence on geometrical parameters

To continue the parameter dependence analysis in the main text, here we discuss the effect of changing the periodicity of the circular grating and the location of the dipole emitter in the polymer layer. Figure S3 represent the intensity angular distributions and collection efficiency for different values of these parameters. The parameters are detuned above and below the optimized parameters ($\Lambda/\lambda_0 = 0.86$ and $d/\lambda_0 = 0.29$). The effect of detuning the periodicity leads to a mismatch between the waveguide propagation constant and the grating Bragg wavevector causing the formation of sidebands. On the other hand changing the dipole location will lead to lower coupling between the dipole emission and the waveguide mode. This will have the primary effect of lowering the radiative enhancement as can be seen from figure S3c. It will slightly change the collection efficiency of the antenna (see figure S3d).